Personalising left-ventricular biophysical models of the heart using parametric physics-informed neural networks

Buoso, Stefano ; Joyce, Thomas ; Kozerke, Sebastian

Abstract: We present a parametric physics-informed neural network for the simulation of personalised left-ventricular biomechanics. The neural network is constrained to the biophysical problem in two ways: (i) the network output is restricted to a subspace built from radial basis functions capturing characteristic deformations of left ventricles and (ii) the cost function used for training is the energy potential functional specifically tailored for hyperelastic, anisotropic, nearly-incompressible active materials. The radial bases are generated from the results of a nonlinear Finite Element model coupled with an anatomical shape model derived from high-resolution cardiac images. We show that, by coupling the neural network with a simplified circulation model, we can efficiently generate computationally inexpensive estimations of cardiac mechanics. Our model is 30 times faster than the reference Finite Element model used, including training time, while yielding satisfactory average errors in the predictions of ejection fraction (-3%), peak systolic pressure (7%), stroke work (4%) and myocardial strains (14%). This physics-informed neural network is well suited to efficiently augment cardiac images with functional data and to generate large sets of synthetic cases for training deep network classifiers while it provides efficient personalization to the specific patient of interest with a high level of detail.

DOI: https://doi.org/10.1016/j.media.2021.102066

Medical Image Analysis 71 (2021) 102066

Contents lists available at ScienceDirect

Medical Image Analysis

journal homepage: www.elsevier.com/locate/media

Personalising left-ventricular biophysical models of the heart using parametric physics-informed neural networks

Stefano Buoso*, Thomas Joyce, Sebastian Kozerke

Institute for Biomedical Engineering, ETH Zurich and University Zurich, Zurich, Switzerland

ARTICLE INFO

Article history:
Received 30 October 2020
Revised 30 March 2021
Accepted 1 April 2021
Available online 20 April 2021

Keywords:
Finite elements
Machine learning
Physics informed neural networks
Personalised cardiac mechanics
Reduced-order models
Shape model

ABSTRACT

We present a parametric physics-informed neural network for the simulation of personalised left-ventricular biomechanics. The neural network is constrained to the biophysical problem in two ways: (i) the network output is restricted to a subspace built from radial basis functions capturing characteristic deformations of left ventricles and (ii) the cost function used for training is the energy potential functional specifically tailored for hyperelastic, anisotropic, nearly-incompressible active materials. The radial bases are generated from the results of a nonlinear Finite Element model coupled with an anatomical shape model derived from high-resolution cardiac images. We show that, by coupling the neural network with a simplified circulation model, we can efficiently generate computationally inexpensive estimations of cardiac mechanics. Our model is 30 times faster than the reference Finite Element model used, including training time, while yielding satisfactory average errors in the predictions of ejection fraction (-3%), peak systolic pressure (7%), stroke work (4%) and myocardial strains (14%). This physics-informed neural network is well suited to efficiently augment cardiac images with functional data and to generate large sets of synthetic cases for training deep network classifiers while it provides efficient personalization to the specific patient of interest with a high level of detail.

1. Introduction

In-silico models of patient-specific cardiac mechanics are based on the solution of multi-physics, nonlinear partial differential equations integrating electrophysiology, fluid dynamics and continuum mechanics (Chabiniok et al., 2016). These models can be personalised upon definition of the anatomy, the microstructure and the characteristics of the circulatory system. In general, this process includes the identification of one or more parameters in an iterative process that requires multiple complete runs of the multi-physics model (Pfaller et al., 2019; Mollro et al., 2019). Once the parameters have been determined, the model offers the assessment of cardiac function for multiple physiological scenarios of interest (Corral-Acero et al., 2020). In-silico models can also be used to generate training data for neural networks and to augment existing datasets with realistic synthetic images, for example by combining the anatomical model with conditional image synthesis (Joyce and Kozerke, 2019; Abbasi-Sureshjani et al., 2020). These applications might require hundreds or thousands of runs of the same model. Despite the increase in available computational power, the large dimension of the model and its intrinsic nonlinearity mean that each of the solutions requires considerable computational resources and long computing times. Therefore, the generation of left-ventricular functional models from patient-specific anatomical data remains prohibitive for most practical applications of interest.

Different abstraction levels can be used to balance the computational cost of the in-silico model against the level of detail. Lumped-parameter models (Charlton et al., 2019) provide an approximation of the physics with a considerable reduction of computational time and complexity. These methods are commonly used to represent the interaction between the heart and the circulatory system, and also bulk heart dynamics (Caruel et al., 2014). However, they greatly simplify the physics and do not allow for a sufficient level of personalisation to the specific patient.

An alternative approach, provided by parametric reduced-order models (ROMs), aims at reducing the cost associated with the solution of the full order model (FOM). ROMs have been extensively studied in the last decade in the context of fluid dynamics (Buoso et al., 2019; Manzoni et al., 2012; Quarteroni and Rozza, 2007; Rowley, 2011) and, to a lesser extent, for structural dynamics and

* Corresponding author.
E-mail address: buoso@biomed.ee.ethz.ch (S. Buoso).

https://doi.org/10.1016/j.media.2021.102066

fluid-structure interaction (Buoso and Palacios, 2017; Pfaller et al., 2020). An important feature of ROM approaches is that they can account for parameter variations: this is mandatory in clinical applications due to the intrinsic variability of anatomical and physiological features in the population. ROMs are commonly based on the definition of a set of radial bases with lower dimensionality than the original system onto which the nonlinear FOM description is projected. It is essential to identify the expected variability to ensure that the radial bases can accurately represent all possible scenarios. While these approaches have shown good predictive features (Buoso et al., 2019), they often require access to matrices and solution structures of the FOM solver (intrusive approaches) which is difficult or even not possible with commercial software.

Recently, non-intrusive approaches based on neural networks have been developed. Hesthaven and Ubbiali (2018) and Del Santo et al. (2020) proposed to learn the correlation between the weights of the radial bases and boundary conditions using a supervised learning approach. In these works, the radial basis functions correspond to the last, non-trainable layer of the network. Lee and Carlberg (2020) and Fresca et al. (2020) exploited convolutional autoencoders for the derivation of nonlinear low-order subspaces for ROMs. The system dynamics are also approximated with neural networks, which are trained simultaneously with the autoencoders.

In the present work we propose a physics-informed neural network (PINN) that can be personalised for each patient and provides fast and reliable estimations of cardiac function. It can generate a functional cardiac model from anatomical clinical images at an affordable computational cost and in a fraction of the time when compared to standard Finite Element (FE) solvers. As in Hesthaven and Ubbiali (2018); Del Santo et al. (2020), the aim is to design a network to predict the amplitude of a set of radial basis functions encoding preselected deformation features of left-ventricular mechanics. These are computed using Proper Orthogonal Decomposition (POD) on a dataset of synthetic cardiac deformations obtained from a parametric FE biophysical model. The FE model is based on a parametric shape model (SM) obtained from high fidelity cardiac images. The SM provides a uniform and consistent framework to compare different anatomies and simulations and it is the key enabler for the parametric variations used to obtain the radial bases for the neural network. The FM allows for representation of cardiac deformations using a low-rank approximation, which reduces the size of the PINN.

The parametrization of left-ventricular anatomies has also been very recently used by Maso Talou et al. (2020) in conjunction with neural networks. Using Principal Component Analysis on a set of left-ventricular anatomies, they derived a low-order representation which was then provided as input to a set of Siamese networks trained using a supervised approach to simulate diastolic left-ventricular function. In their approach, the networks are trained only once but they require the availability of a reference solution dataset from a biophysical model. Additionally, left-ventricular mechanics is only restricted to the diastolic phase.

Instead of having to compute input-output pairs for supervised network training, we adopt a custom cost function that encodes the minimization of the potential energy of the cardiac problem (Raissi, 2018; Nguyen-Thanh et al., 2020). Our cost function is specifically designed to include the effect of the microstructure of the heart and the active contraction resulting from myocytes activation. In this way we can simulate full cardiac cycles and avoid expensive FE simulations for the training of the network for each new patient of interest. To the authors' knowledge, this is the first time physical constrains are enforced in two complementary ways simultaneously. Firstly, by using POD radial basis functions, the solution is forced to belong to a prescribed linear subspace representing left ventricular dynamics. Secondly, the cost function penalises deformations that do not satisfy momentum conservation equations.

We present the key methodological aspects in Section 2 including the generation of the SM, the biophysical FE model, the POD radial basis subspace and the network architecture. We then compare the predictions of the proposed PINN relative to the conventional FE model using metrics of clinical interest, such as ejection fraction, maximum ventricular systolic pressure, net ventricular work and myocardial strains.

2. Methods

The personalized model proposed in this work hinges on two sets of radial basis functions. The first set, the shape model (SM, Fig. 1, block I), is derived from high-resolution cardiac images and it provides an approximations of left-ventricular anatomies. The SM allows us to standardise the setup of the FE model and to implement a common structure for processing cardiac deformations. The generation of the SM is described in Section 2.1. The shape model does not contain information on shape torsion and twisting, so it can not approximate deformations over the cardiac cycle. For this reason, we also build a second set of basis functions, the functional model (FM, Fig. 1, block II), obtained from the displacement fields of left-ventricular anatomies computed with the biophysical FE model. The generation of the FM is described in Section 2.2. The FM bases will define the non-trainable, physics-based final layer of the PINN. All other layers can be trained for each patient-specific anatomy at a low computational cost (Fig. 1, block III) as described in Section 2.3.

2.1. Left-ventricular shape model

The left-ventricular shape model is derived from high resolution cardiac Magnetic Resonance (MR) and Computed Tomography (CT) images of the Multi-Modal Whole Heart (MMWH) dataset (Zhuang and Shen, 2016; Zhuang, 2013; Zhuang et al., 2010). MRI images were acquired on a 1.5 T clinical scanner (Philips Healthcare, Best, The Netherlands) using a balanced steady state free precession (b-SSFP) turbo field echo (TFE) sequence. All the data was acquired at $2 \times 2 \times 2mm^3$ and reconstructed to $1 \times 1 \times 1mm^3$. Contrast enhanced cardiac CT data was obtained using a standard coronary CT angiography protocol on clinical scanners (Philips Healthcare, Netherlands) with a resolution of $0.44 \times 0.44 \times 0.60\text{mm}^3$. The dataset includes a single cardiac phase from healthy patients and subjects with cardiovascular disease all aged between 5 and 80.

Left-ventricular anatomies up to the mitral valve plane are obtained from 75 cases of the dataset. Of these, 40 cases (20 CT and 20 MRI) already had masks provided with the data, while the other 35 MRI cases were processed using a U-Net based segmentation model (Ronneberger et al., 2015), which was trained to segment the left ventricle in short-axis slices using labelled data from MMWH and the Automated Cardiac Diagnosis Challenge (Bernard et al., 2018). Our network was implemented in Keras (Chollet et al., 2015) using the Tensorflow backend (Abadi et al., 2015), and trained on a single Titan X GPU. Training takes approximately 1.5 h, after which the labels for the 35 additional cases can be predicted in approximately 5 s.

All shapes are manually corrected and cut with a plane passing from just below the aortic tract and approximately parallel to the mitral valve plane. Finally, endocardium, epicardium and the coordinates of apex and inferior intersection between left and right ventricles are identified. For each anatomy, a shape-adapted physiological parametrization (PP) is defined. It approximates the prolate ellipsoid radial, circumferential and longitudinal coordinates (Toussaint et al., 2013). In detail, the transmural coordinate is set

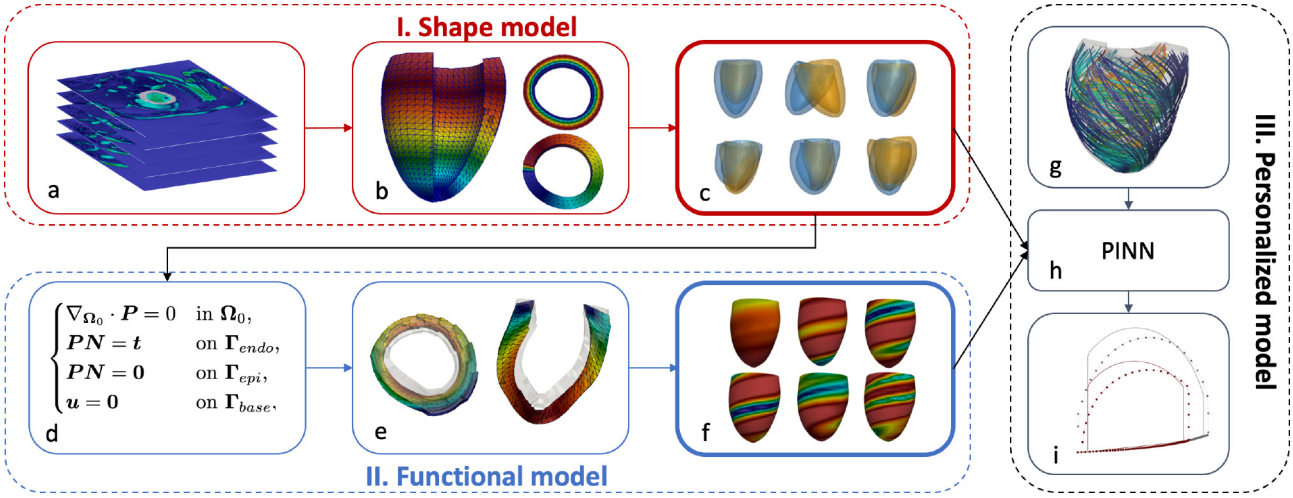

Fig. 1. The methodological steps are schematically shown here split in three main blocks: generation of the shape model (I), generation of the functional model (II) and definition of the personalised biophysical left ventricular model (III). In block I left-ventricular anatomies are extracted from medical data (a) and mapped with a physiological parametrization which is used for generating meshes with inter-anatomy consistency (b). By applying POD we then obtain the basis functions of the SM (c). In block II we use the variability observed in the medical images to generate synthetic anatomies with the SM and define realistic operative conditions using a biophysical finite element model (d). We obtain a dataset of anatomical deformations (e) and POD is then used to construct the FM (f). In block III a personalised model is generated for each case of interest: starting from medical images we can extract the left-ventricular anatomy (or alternatively generate a realistic one using the SM), prescribe micro-structure, tissue properties and systemic circulation parameters (g). The personalised PINN is trained (h) for the prediction of left ventricular deformations and function (i). (For interpretation of the references to colour in this figure legend, the reader is referred to the web version of this article.)

to 0 and 1 for all points at the endocardium and epicardium, respectively. An Eikonal problem (Fares and Schröder, 2002) is solved on the endocardium and epicardium to compute the distance of each point from the apex. Endocardium and epicardium are then mapped on the unit disc centered at the origin of a Cartesian coordinate system (Paun et al., 2017) imposing the mapping of the inferior intersection point to the position (1,0) and of the apex to the disc center. The circumferential coordinate of the surfaces is obtained from the angular positions of the points on the discs. The longitudinal coordinate is given by the distance from the apex normalised by the maximum distance at the same angular position. Physiological directions in the radial, longitudinal and circumferential directions are obtained from the normalised gradient directions of the corresponding scalar parametric field.

The PP is then used to map a reference tetrahedral mesh built on a unit disc onto each of the anatomies considered. For the disc, the PP is simply obtained by the cylindrical coordinates of the points. This approach ensures that all meshes have the same number of nodes and it preserves the mesh connectivity and the anatomical correspondence between the different cases. Additionally, the calculation of the longitudinal coordinate with the Eikonal model ensures reduced distortion of the mesh elements during mapping. For the specific application in this work, the reference mesh is generated using 40, 30 and 4 nodes in the circumferential, radial and height directions, respectively, for a total of 4804 nodes and 21,240 tetrahedral elements. This results in 40, 30 and 4 nodes in the circumferential, longitudinal and radial directions of the anatomies.

All meshes are then translated to centre the encodardium contour at the cut plane to the origin of the Cartesian coordinate system, rotated to align the plane normal to the positive z axis and place the inferior intersection point on the negative x axis. For each anatomy, we generate a *snapshot* defined as a column vector containing mesh nodal coordinates and vectors of the physiological directions. Proper Orthogonal Decomposition (POD) is applied as in Buoso et al., 2019, 2020 to the set of snapshots to extract thebases that gives the optimal linear approximation of the set in a least square sense. Thus, when applying POD, we obtain the bases to reconstruct both the anatomy and the local physiological directions simultaneously (Buoso et al., 2020; Joyce et al., 2020). The bases are ordered in decreasing order of contribution to the total variance of the input dataset. The SM projection matrix is $\boldsymbol{\Psi}_0 = [\psi_1 \dots \psi_M]$, where the ith column, ψ_i, is the ith basis computed with POD. The number of basis, M, determines the accuracy of the approximation (Buoso et al., 2019). The coordinates of the nodes of each mesh, $\boldsymbol{X}$ can be approximated as $\boldsymbol{X} \approx \boldsymbol{\Psi}_0 \boldsymbol{a}$ where the vector of modal amplitudes becomes the parametric representation of the mesh in the selected POD subspace. Thanks to the inclusion of the local direction vectors in the snapshots, each physiological direction can be similarly reconstructed. This approach generates an anatomical low-dimensional representation that captures the dominant modes of variation of the high-dimensional training dataset. Synthetic realistic geometries can be generated by sampling a vector of amplitudes for the SM bases (Joyce et al., 2020).

2.2. Biophysical and functional models

The FE biophysical model for the left ventricle is based on the finite deformation framework (Bonet, 2001; Bonet and Wood., 2008; Simo and Hughes, 1998). Let $\boldsymbol{\Omega}_0$ be the initial reference configuration of the left ventricle with boundaries $\boldsymbol{\Gamma}_{endo}$, $\boldsymbol{\Gamma}_{epi}$, and $\boldsymbol{\Gamma}_{base}$ being the endocardium, epicardium and base, respectively. Given a deformed configuration, $\boldsymbol{\Omega}$, the deformation gradient is defined as $\boldsymbol{F} = \nabla \boldsymbol{u} + \mathbb{I}$ where $\boldsymbol{u}(\boldsymbol{X}, t)$ is the displacement field and $\mathbb{I} \in \mathbb{R}^{3\times 3}$ is the identity tensor. The deformation gradient $\boldsymbol{F}$ is decomposed into its volumetric and isochoric components (Bonet, 2001) so that $\boldsymbol{F}_{iso} = \boldsymbol{F} J^{-\frac{1}{3}}$ represents the isochoric deformation and $J = \det(\boldsymbol{F})$ measures changes in volume. The deformation of the left ventricle is determined by the equilibrium of the passive stresses generated by the pressure loading at the endocardium and the active contraction of the myocytes. The passive mechanical response is defined using the quasi-incompressible formulation of the anisotropic strain energy function, $\mathcal{W}_p$, proposed by Holzapfel and Ogden (2009):

$$
\begin{aligned}
W_p(\boldsymbol{C}, J) = & \frac{a}{b}\left[e^{b(I_1-3)} - 1\right] + \frac{a_f}{2b_f}\left[e^{b_f\left(I_{4,f}-1\right)^2} - 1\right] \\
& + \frac{a_s}{2b_s}\left[e^{b_s\left(I_{4,s}-1\right)^2} - 1\right] + \frac{a_{fs}}{b_{fs}}\left[e^{b_{fs} I_{8,fs}^2} - 1\right] \\
& + \frac{K}{2}\left(J^2 - 1\right)^2, \qquad (1)
\end{aligned}
$$

where a, b, a_f, b_f, a_s, b_s, a_{fs} and b_{fs} are material coefficients, K is the bulk modulus penalising volume variations and

$$\begin{aligned} I_1 &= J^{-\frac{2}{3}}\mathrm{tr}\boldsymbol{C}, & I_{4,f} &= J^{-\frac{2}{3}}\boldsymbol{f}_0\cdot\boldsymbol{C}\boldsymbol{f}_0, \\ I_{4,s} &= J^{-\frac{2}{3}}\boldsymbol{s}_0\cdot\boldsymbol{C}\boldsymbol{s}_0 & I_{8,fs} &= J^{-\frac{2}{3}}\boldsymbol{f}_0\cdot\boldsymbol{C}\boldsymbol{s}_0, \end{aligned} \tag{2}$$

are the invariants of $\boldsymbol{C}=\boldsymbol{F}^T\boldsymbol{F}$ and $\boldsymbol{f}_0\in\mathbb{R}^{3\times1}$ and $\boldsymbol{s}_0\in\mathbb{R}^{3\times1}$ are the local fibres and sheet directions of the heart tissue in the reference configuration $\boldsymbol{\Omega}_0$.

The active contribution to the stresses determined by the contraction of the myocytes is defined with the potential function (Finsberg, 2017)

$$\mathscr{W}_a = \frac{T_a}{2J}\Big[\big(I_{4,f}-1.0\big)+\eta(I_{4,s}-1.0)+\eta(I_{4,n}-1.0)\Big], \tag{3}$$

where T_a is the stress in the fibre direction, η is a coefficient in the range [0,1] that accounts for the contribution of the stress in the cross fibres directions and $I_{4,n}=J^{-\frac{2}{3}}\boldsymbol{n}_0\cdot\boldsymbol{C}\boldsymbol{n}_0$ where $\boldsymbol{n_0}$ is the direction normal to fibres and sheets. The value of T_a is usually determined from electrophysiological models (Roth and Wikswo, 1986; Potse et al., 2006; Neic et al., 2017). However, Finsberg et al. (2018) and Balaban et al. (2017) have used an averaged fibre stress approach to analyse in-vivo patient cardiac data and showed good discriminating properties of such global metric. To simplify the model in this work, we consider a uniform activation of the myocytes and prescribe the time evolution of T_a using a fourth-order polynomial. The stress tensor in the deformed configuration, $\boldsymbol{\sigma}$, is given by the Cauchy stress tensor as

$$\boldsymbol{\sigma}_p = J^{-1}\boldsymbol{F}^T\boldsymbol{S}\boldsymbol{F}. \tag{4}$$

where $\boldsymbol{S}=2\frac{\partial\mathscr{W}}{\partial\boldsymbol{C}}$ is the second Piola–Kirchhoff stress tensor defined in $\mathbb{R}^{3\times3}$ and $\mathscr{W}=\mathscr{W}_p+\mathscr{W}_a$.

The momentum balance equation, in the reference configuration, neglecting body forces and inertia effects, reads:

$$\begin{cases} \nabla_0\cdot\boldsymbol{P}=0 & \text{in } \boldsymbol{\Omega}_0, \\ \boldsymbol{P}\boldsymbol{N}=\boldsymbol{t} & \text{on } \boldsymbol{\Gamma}_{endo}, \\ \boldsymbol{P}\boldsymbol{N}=\boldsymbol{0} & \text{on } \boldsymbol{\Gamma}_{epi}, \\ \boldsymbol{u}=\boldsymbol{0} & \text{on } \boldsymbol{\Gamma}_{base}, \end{cases} \tag{5}$$

where $\boldsymbol{P}=J\boldsymbol{\sigma}\boldsymbol{F}^{-T}\in\mathbb{R}^{3\times3}$ is the first Piola–Kirchhoff stress tensor, $\boldsymbol{N}\in\mathbb{R}^{3\times1}$ is the surface normal vector and $\boldsymbol{t}$ is the traction stress on the endocardium, $\boldsymbol{\Gamma}_{endo}$, determined by pressure, p_{endo}, generated by the blood pool. In this work, we neglect the effect of the pericardium by applying a zero traction condition at the epicardium, $\boldsymbol{\Gamma}_{epi}$ and we assume a stress-free reference configuration $\boldsymbol{\Omega}_0$ in equilibrium with a zero pressure. We also set to zero the displacement at the cut plane position, $\boldsymbol{\Gamma}_{base}$, Eq. (5) is solved in FEniCs (Alnæs et al., 2015; Logg et al., 2012) using linear tetrahedral elements obtained with the discretisation described in Section 2.1.

During the filling phase, the pressure is linearly increased up to a prescribed end-diastolic value, p_{ED}. For the isovolumetric contraction and relaxation phases, we iteratively solve Eq. (5) to determine the value of p_{endo} that, when combined with the instantaneous actuation stress T_a, preserves the target constraint volume (end-diastolic and end-systolic volumes for the isovolumetric contraction and relaxation, respectively). In our model, the systolic phase starts when p_{endo} exceeds the end-diastolic aortic pressure, p_A, and the pressure values are computed using a two element Windkessel model (Westerhof et al., 2009). When the ventricular volume returns to the initial end-systolic value or the blood inflow is negative, the isovolumetric contraction starts.

An important metric used in this work are physiological strains. Given a deformation field $\boldsymbol{u}$ from the reference configuration $\boldsymbol{\Omega}_0$ to a deformed state $\boldsymbol{\Omega}$, the Lagrangian strain tensor is defined as $\boldsymbol{E}=\frac{1}{2}(\boldsymbol{C}-\mathbb{I})$. The physiological strain, e_i in one of the physiological directions $\boldsymbol{v}_i$ is obtained as $e_i=\boldsymbol{v}_i^T\boldsymbol{E}\boldsymbol{v}_i$. In our work we consider strains in the radial, longitudinal and circumferential directions defined by the PP, as e_r, e_l and e_c, respectively.

The biophysical FE model can be used to obtain a dataset of left-ventricular deformations for given left-ventricular anatomical, mechanical, micro-structural and functional variations. Specifically, anatomical variability is prescribed using the SM. The SM basis accounting for 99% of the energy observed and in the MMWHS dataset (Buoso et al., 2019) are used to generate 100 synthetic of FE anatomical configurations, $\boldsymbol{\Omega}_0$, by uniform-randomly sampling the corresponding amplitudes within the range boundaries of the SM (Young and Frangi, 2009). Passive material properties for the model of Eq. (1) are taken from (Sack et al., 2018) and, for each synthetic anatomy, the values a, a_f, a_s, a_{fs} are randomly scaled by a factor D in the range [0.5,1.5]. The bulk modulus, K, is set to 100 times the values of a_f. Linear transmural laws are used for the definition of the fibre directions (Carruth et al., 2016). Epicardium, α_{epi}, and endocardium, α_{endo}, helix angles are randomly selected in the range [60°, 30°] and [40°, 75°], respectively. The transmural angles of fibres and sheets are 0° and 65°, respectively, for all anatomies. For Eq. (3), maximum active stress values, T_a, range between 10 kPa and 200 kPa and η is set to 0.3 for all cases. The active stress is identically zero during diastole and, during systole, it is scaled by a fourth-order polynomial with a peak at half systole. The resistance, R, and capacitance, C, of the Windkessel model for the systemic circulation are 50.0 $\frac{\text{Pa}\cdot\text{s}}{\text{ml}}$ and 5.5 $\frac{\text{mm}^3}{\text{kPa}}$, respectively. The values of end diastolic pressure, p_{ED}, and aortic diastolic pressure, p_A, are 20 mmHg and 70 mmHg, respectively. Simulations start at beginning of diastole and have a duration of 950 ms. Diastole is set to 650 ms, while the duration of the other phases depend on the value of the maximum active stress and the interaction of the left ventricle with the systemic circulation. Simulated deformations are discarded if the ejection fraction and peak systolic pressure are not in the pre-selected range [0.3–0.8] and [50–150]mmHg, respectively. Additionally, we also ensured that the volume is monotonically increasing during diastole, and decreasing during systole. If a simulation is discarded, a new one is considered until these criteria are met. For each anatomy, the simulated displacement fields from 30 equally spaced frames are stored and used to build the FM projection matrix as $\boldsymbol{\Phi_u}=[\varphi_1\dots\varphi_N]$ using POD. The FM allows the definition of a low-rank representation of the displacements of the dataset used for POD analysis. It implicitly encodes the modelling assumptions used for the generation of the snapshots.

2.3. Physics informed neural network

We propose to use a dense neural network as an anatomy-specific solver to calculate the vector of the amplitudes, $\boldsymbol{a_u}$, such that the predicted displacement, $\boldsymbol{u}=\boldsymbol{\Phi_u}\boldsymbol{a_u}$ satisfies Eq. (5) with p_{endo} and T_a as inputs. As for the FEM model, inertial effects are neglected and quasi-static solutions are sought. The total number of hidden layers and their size can be selected during the design of the network. The only requirement is that the layer before the linear projection must have N neurons, where N is the number of columns of the FM. The final layer is non-trainable and projects the $\boldsymbol{a_u}$ prediction from the network (using fixed weights $\boldsymbol{\Phi_u}$) to the displacement field of the left ventricle, $\boldsymbol{u}$ defined at each mesh node. The network structure is shown in Fig. 2.

The cost function to be minimised with the training is the potential energy functional (Bonet, 2001)

$$\mathscr{J}=\int_{\boldsymbol{\Omega}_0}\mathscr{W}dV-\int_{\boldsymbol{\Gamma}_{endo}}\boldsymbol{t}\cdot\boldsymbol{u}dA, \tag{6}$$

where $\boldsymbol{t}$ are the traction forces acting on the boundaries, which, in our case, are determined by the pressure acting on the endocardium. The solution to Eq. (5) corresponds to the solution of the minimization problem of the functional (6).

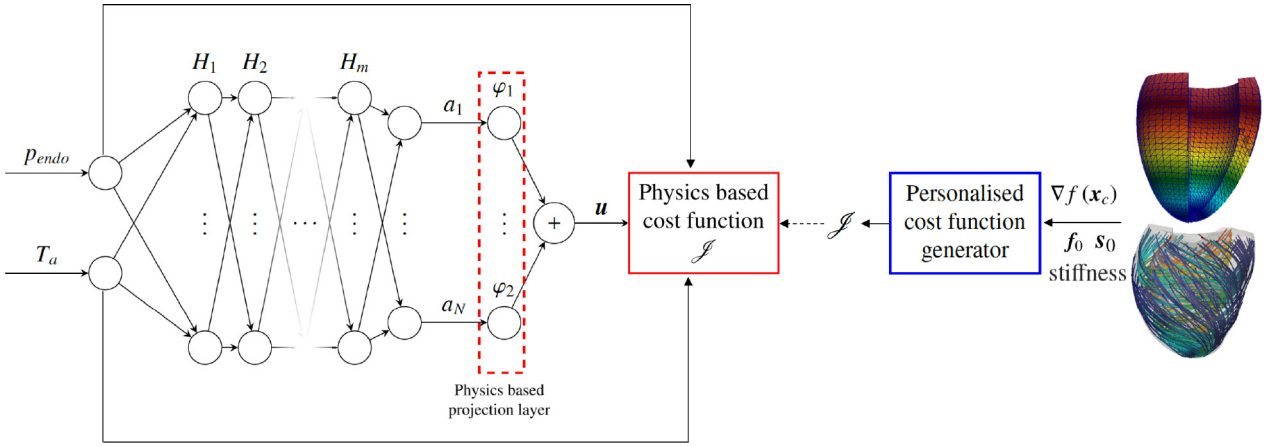

Fig. 2. High level structure of the neural network. The input layer consists of the instantaneous values of the pressure at endocardium, p_{endo}, and actuation stress, T_a. We use m dense hidden layers, $H_1, \dots, H_m$, with k neurons and trainable weights and biases. The output layer predicts the amplitudes $\boldsymbol{a_u} = [a_1, \dots, a_N]$ of the FM modes, $\boldsymbol{\Phi_u} = [\varphi_1, \dots, \varphi_N]$, which are the input to the projection layer, with non-trainable parameters, resulting in the discrete displacement field $\boldsymbol{u}$ for all vertices of the mesh. The displacements $\boldsymbol{u}$ are used to compute the cost function $\mathscr{J}$ during training. We note that p_{endo} and T_a are also given in the cost function. The PINN is personalised to the case of interest generating the cost function from the gradient operator defined on the anatomy, the microstructure and the tissue stiffness. (For interpretation of the references to colour in this figure legend, the reader is referred to the web version of this article.)

The calculation of the first term of the cost function requires us to compute the gradient of the displacement field in the reference configuration, $\nabla \boldsymbol{u}$. We use the approach from Mancinella et al. (2019) for the estimation of the gradient of a scalar function, $f(\boldsymbol{x})$, defined on the nodes of tetrahedral meshes. In our case $f(\boldsymbol{x})$ can be any of the components of the displacement field vector. The gradient at the centroid of a tetrahedral element with vertices $\boldsymbol{v}_i, \boldsymbol{v}_j, \boldsymbol{v}_k, \boldsymbol{v}_l$ can be computed as

$$\begin{bmatrix} \boldsymbol{v}_j - \boldsymbol{v}_i \\ \boldsymbol{v}_k - \boldsymbol{v}_i \\ \boldsymbol{v}_l - \boldsymbol{v}_i \end{bmatrix} \begin{bmatrix} \nabla f(\boldsymbol{x}_c)_x \\ \nabla f(\boldsymbol{x}_c)_y \\ \nabla f(\boldsymbol{x}_c)_z \end{bmatrix} = \begin{bmatrix} f(\boldsymbol{x}_j) - f(\boldsymbol{x}_i) \\ f(\boldsymbol{x}_k) - f(\boldsymbol{x}_i) \\ f(\boldsymbol{x}_l) - f(\boldsymbol{x}_i) \end{bmatrix}, \tag{7}$$

where $\boldsymbol{v}_p = (x_p, y_p, z_p)$ is the vector of coordinates of node p and $\nabla f(\boldsymbol{x}_c) = (\nabla f(\boldsymbol{x}_c)_x, \nabla f(\boldsymbol{x}_c)_y, \nabla f(\boldsymbol{x}_c)_z)$ is the gradient at the cell centroid, $\boldsymbol{x}_c$. The gradient at each node is then computed as the weighted volume averaged of all the elements that contain that node. The matrices can be precomputed and assembled in a global matrix such that the nodal gradient can be obtained as the product of the global matrix and the vector of the selected component of the displacement field of the points. We excluded from the assembly the contribution of the elements containing the apex nodes since their inclusion resulted in inaccurate results due their small size.

In this work, the cost function (6) is computed with respect to the reference configuration $\boldsymbol{\Omega}_0$. As a result, the matrix for the gradient computations is a function of the initial anatomy and not of the displacement field. Thus, it just needs to be assembled once beforehand. Traction forces, $\boldsymbol{t}$, need to be expressed in the reference configuration as well. In our case, they can be expressed as

$$\boldsymbol{t} = -J p_{endo} \boldsymbol{N} \boldsymbol{F}^{-T} dA, \tag{8}$$

where $\boldsymbol{N}$ and dA are the normal and the area of the faces of the elements belonging to the endocardium, respectively, in the reference configuration $\boldsymbol{\Omega}_0$.

Specifically for this work, all PINN hidden layers have a number of neurons equal to the number of selected FM bases. A *swish* activation function (Ramachandran et al., 2017) is used on every hidden layer, except for the last trainable one. The network is trained with 400 input conditions, i.e (p_{endo}, T_a) tuples, considering a tensor grid sampling for p_{endo} and T_a in the range [0,150 mmHg] and [0,100 kPa], respectively. We use the Adam optimizer (Kingma and Ba, 2014) and train the system for 300 epochs with a learning rate of $1e^{-4}$ on a single CPU (Intel(R) Core(TM) i7-8700, 3.20 GHz). Network design and training use the libraries from Tensorflow (Abadi et al., 2015). The PINN can be thought of as a solver that maps each input pair to a deformed configuration satisfying (5). Such a map is learned during training, and can then provide instantaneous deformation predictions for any input pair within the upper and lower bounds of p_{endo} and T_a seen during training.

We summarise here the sequence of steps involved in the generation of the personalised model and its use (refer to Fig. 2):

[1] Define a mesh using medical images or directly with the SM. The resulting mesh must be parametrized (Section 2.1) and projected onto the SM.
[2] Define microstructure, stiffness and expected ranges of p_{endo} and T_a.
[3] Construct the gradient operators on the mesh with Eq. (7).
[4] Steps **[1]**–**[3]** provide the building blocks for the calculation of the deformation gradient and of the cost function using Eq. (6).
[5] Build the PINN architecture and use the FM bases as the last layer of the network.
[6] Select the training pairs for the PINN. In our work 400 tuples obtained from the tensor grid sampling of the 2D space in p_{endo} and T_a are used.
[7] Train the PINN minimizing the functional designed in step 4.
[8] The PINN can now be used as a solver that predicts the displacement of the mesh nodes for input values of p_{endo} and T_a. This is specific for the anatomy defined through steps **[1]** and **[2]**. The PINN can be coupled with circulation models to simulate the full cardiac cycle of the left ventricle

For the comparison of the PINN prediction performance against the FE model, 10 additional anatomies are generated selecting SM amplitudes, micro-structure and material properties with the same approach used for building the FM (Section 2.2). For each anatomy the PINN is trained and used to simulate six different operative conditions by varying reference pressure values, maximum actuation stress and parameters of the systemic circulation, for a total of 60 cases used for the calculation of the error statistics. We compare the predictions of the biophysical FE model and the PINN with different numbers of FM bases. The minimum number of bases is set such that at least 95% of the total energy of the deformation dataset is captured (Buoso et al., 2019). Although the optimization of the PINN architecture is beyond the scope of this work, we also

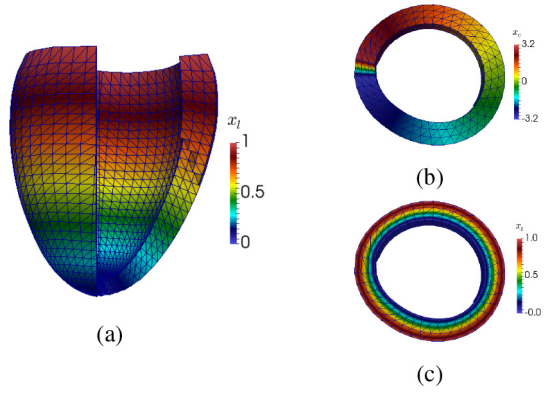

Fig. 3. Average left ventricle SM mesh and longitudinal parameter (a), circumferential parameter (b) and transmural parameter (c). (For interpretation of the references to colour in this figure legend, the reader is referred to the web version of this article.)

investigate the variation of the PINN predictions with 5 and 7 hidden layers.

The code for PINN training, including the SM and FM bases used in this work, is publicly available at https://github.com/sbuoso/Cardio-PINN/ under MIT license conditions.

3. Results

3.1. Shape and functional models

The average mesh of the SM is shown in Fig. 3a–c display the longitudinal, circumferential and transmural parameters, respectively. Fig. 4 shows the first four SM bases derived with POD, which account for approximately 99% of the total energy in the dataset and 80% of the observed variance. We present the impact of each basis on the final anatomy by visualizing the mode weighted by the maximum (blue) and minimum (orange) computed amplitudes added to the mean shape.

The first 4 SM bases are therefore used to generate the synthetic anatomies for the generation of the FM.

Similarly to the SM, the functional model is characterised by a quick decrease of the impact of each base, with the first 5 accounting already for 95% of the total energy of the system and for 85% of its variance. Here, we compare PINNs using 5, 10, 15 and 20 FM bases.

3.2. Physics informed neural network

The 60 test simulation (6 operative conditions for each of the 10 test anatomies) are simulated with the FE model which provides the ground-truth for the anatomical deformations and the metrics of cardiac function. The variation of the operative conditions is obtained by coupling the anatomy to different circulation models and selecting different maximum actuation values. The range of ejection fractions, EF, peak systolic pressures, PSV, and stroke work, W_{stroke}, are [0.3–0.5], [37.0–125.0] mmHg and [0.01–0.7] W, respectively. The range of EF obtained goes from severe left-ventricular dysfunction to the boundary of physiological conditions.

Fig. 5 show the error statistics for the predictions of PINN and FE models for EF, PSV and W_{stroke}. Errors are computed from the 60 total cases generated for the comparison and they are presented as mean and standard deviation.

The mean and standard deviation for EF errors for $m = 5$ (Fig. 5a) significantly reduce when increasing the number of FM bases, N, from 5 to 10 (from -0.25 ± 0.21 to -0.03 ± 0.05, respectively). A further increase in dimension slightly worsen EF prediction with errors of -0.09 ± 0.08 and -0.12 ± 0.07 for $N = 15$ and 20, respectively. An increase in the number of hidden layers, m, from 5 to 7 worsen prediction performance for $N = 5$, increasing the mean error to 0.29 with a variance of 0.17. For larger N values, mean errors are reduced, but larger standard deviation are observed. With 7 hidden layers, error statistics are -0.01 ± 0.09, -0.03 ± 0.10, -0.09 ± 0.08 for $N = 10, 15$ and 20, respectively.

PSV errors are shown in Fig. 5b. For $m = 5$, errors are 0.06 ± 0.07, 0.07 ± 0.06, 0.13 ± 0.05, 0.16 ± 0.06 for $N = 5$, 10, 15 and 20, respectively. Error statistics are almost unchanged when considering 7 hidden layers.

W_{stroke} errors (Fig. 5c) exhibit a similar trend to those of the EF errors. An initial improvement in both mean and standard deviation of the error is observed for $m = 5$ when N is increased from 5 to 10, from -0.12 ± 0.17 to $+0.04 \pm 0.14$, respectively. Further increasing N results in higher means and standard deviations of the errors (0.15 ± 0.14 and 0.23 ± 0.15 for $N = 15$ and 20, respectively. As was also the case for PSV errors, an increase of m from 5 to 7 has little effect on W_{stroke} predictions.

Prediction differences between the two models for radial, e_r, longitudinal, e_l, and circumferential, e_c, strains, respectively are shown in Fig. 6a–c. All three cases show error statistics which are only slightly affected by the PINN depth and number of FM bases. Error statistics show a minimum for $N = 5$ and $m = 5$, with values of -0.09 ± 0.07, -0.06 ± 0.05, -0.12 ± 0.11 for e_r, e_l and e_c, respectively. Increasing N to 10 sets the error statistics to -0.13 ± 0.12, -0.11 ± 0.09, -0.14 ± 0.13 for e_r, e_l and e_c, respectively, with almost no variations for further increases of N.

The calculation of one single operative condition with the FE model takes approximately 2.5 h on a single core (Intel(R) Core(TM) i7-8700, 3.20 GHz), while it takes only 4 min for the PINN, including training time, on the same hardware. We note that the PINN must be trained only once when multiple operative conditions are considered for the same anatomy.

Fig. 7 compares the the pV loop predictions from PINN and FEM for two of the 10 comparison anatomies and two sets of operative conditions. They show representative differences between the two models that are coherent with the statistics presented in Fig. 5. Fig. 8 presents the comparison of the three-dimensional deformation predictions for cases 2 and 4 of Fig. 5.

4. Discussion

We have proposed a physics informed neural network (PINN) embedding physical constrains of cardiac mechanics both in the network architecture and in the cost function used for the training. The network is a biophysical solver that predicts deformations of personalized left-ventricular anatomies from the values of left-ventricular pressure, p_{endo} and actuation force, T_a generated by the myocyte contraction. The PINN does not require the expensive generation of input-output pairs for training and it hinges on the use of two sets or radial basis functions defining shape (SM) and functional (FM) models.

The left-ventricular SM is generated from high-resolution cardiac MR and CT images and it ensures anatomical correspondence of all shapes and results. It uses a shape-adapted physiological parametrization to map a reference mesh to all anatomies of the dataset with limited mesh distortion (Fig. 3). Proper Orthogonal Decomposition (POD) is used to extract the dominant anatomical features in the dataset. The rapid decay of the contribution of the POD bases in Fig. 4f shows that the main global anatomical variations in the original dataset can be represented by a low number of basis and that each basis encodes very distinctive features: global scaling (base 1), base angle tilting (bases 2, 3), thickening of the wall (basis 4) and so on. Such features are consistent with those reported in previous studies on left ventricular shape analysis (Farrar et al., 2016; Suinesiaputra et al., 2018).

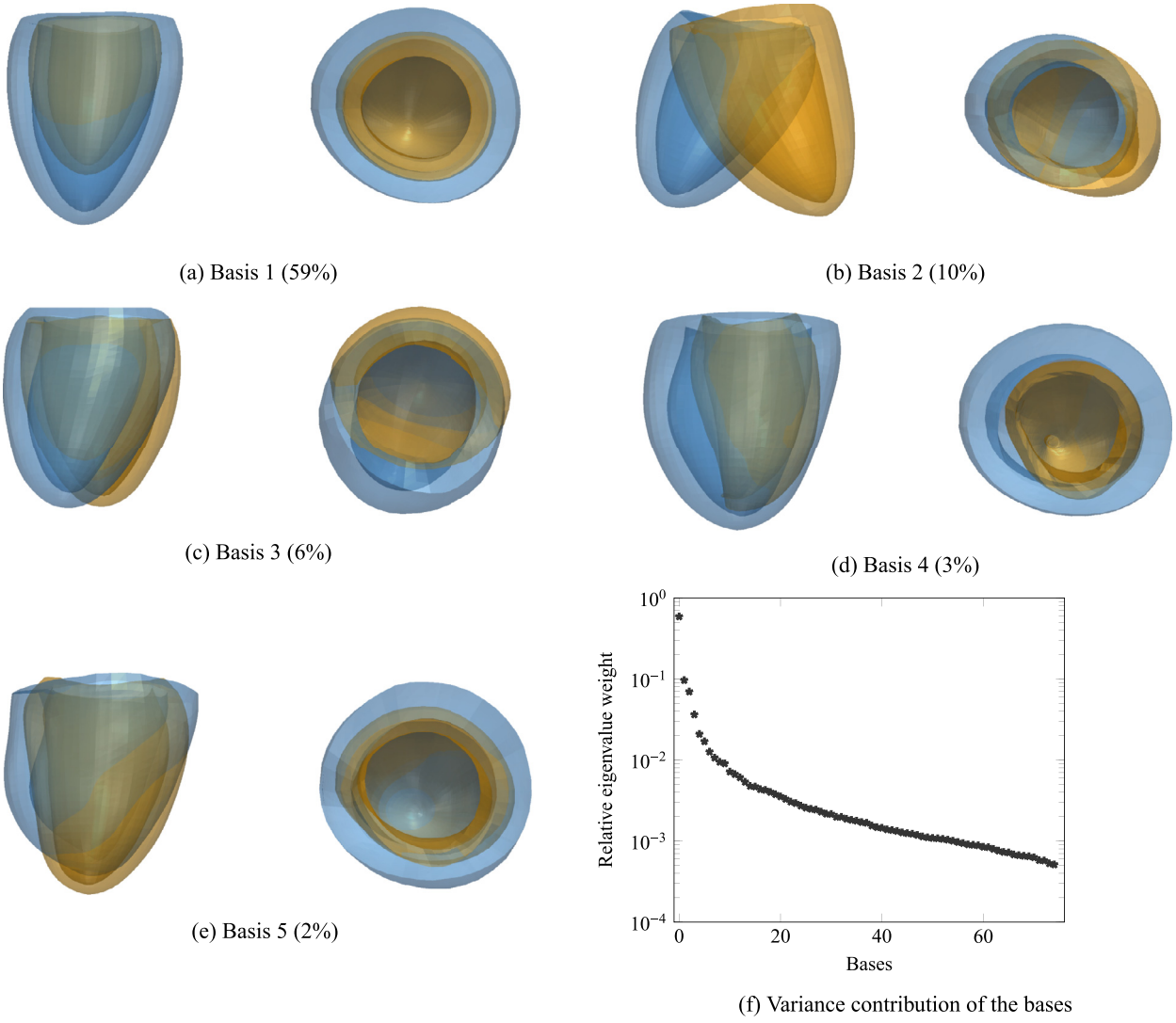

Fig. 4. Long and short axis views of the effects of SM bases from 1 to 5. For each panel the corresponding basis weighted by the maximum (blue) and minimum (orange) amplitudes from the MMWHS dataset are added to the mean shape. The values in brackets refer to the variance represented by each base. The contribution of each basis to the total variance is shown in panel f. (For interpretation of the references to colour in this figure legend, the reader is referred to the web version of this article.)

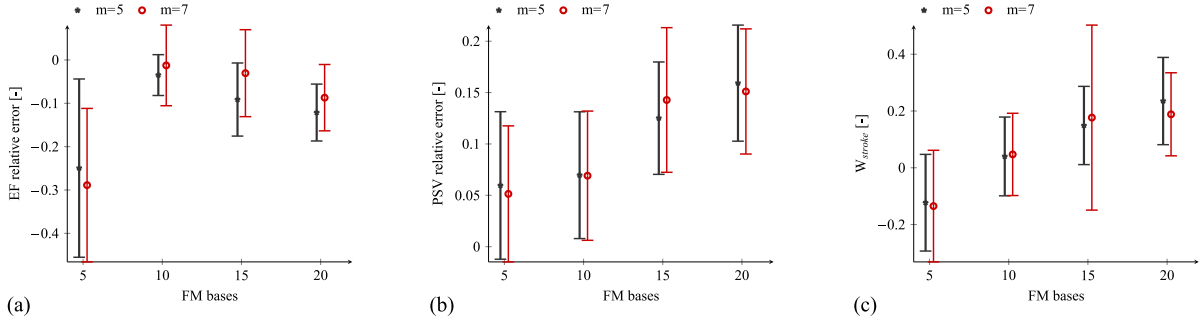

Fig. 5. Relative errors (with sign) on predicted EF (a), PSV (b) and SW (c) between PINN and FEM solutions as function of FM bases and number of hidden layers ($m = 5$ for the black stars, $m = 7$ for red circles). Vertical bar represents ± one standard deviation of the error values. (For interpretation of the references to colour in this figure legend, the reader is referred to the web version of this article.)

An innovative aspect of our SM is that it can efficiently reconstruct local physiological directions together with the anatomy (Buoso et al., 2020). Therefore, once we have identified the amplitudes of the SM basis that match the desired anatomy of interest, we automatically obtain also the PP directions. This can be efficiently done using a neural network as in Joyce et al. (2020). Additionally, we can also randomly select the interpolation weights of the SM bases to generate realistic synthetic anatomies spanning the variability included in the SM training dataset.

The second key aspect of the PINN design is the use of a functional model (FM) providing a low-dimensional representation of

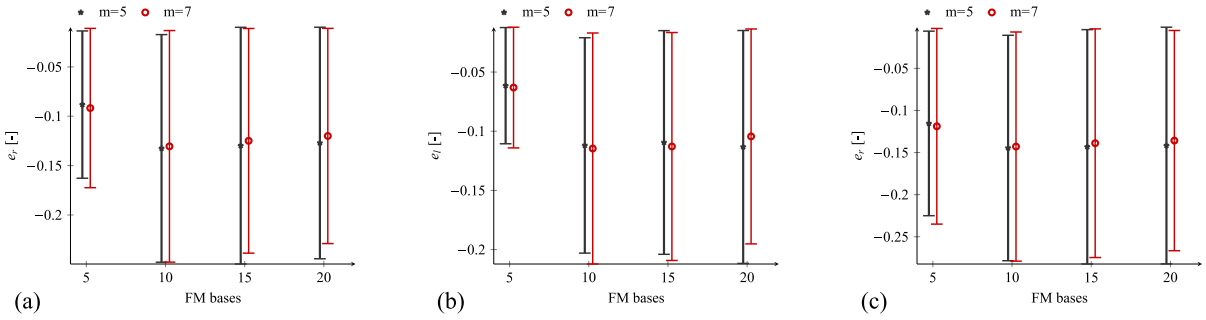

Fig. 6. Relative errors (with sign) on predicted radial (a), longitudinal (b) and circumferential (c) strains between PINN and FEM solutions as function of FM bases and number of hidden layers ($m = 5$ for the black stars, $m = 7$ for red circles). Vertical bar represents ± one standard deviation of the error values. (For interpretation of the references to colour in this figure legend, the reader is referred to the web version of this article.)

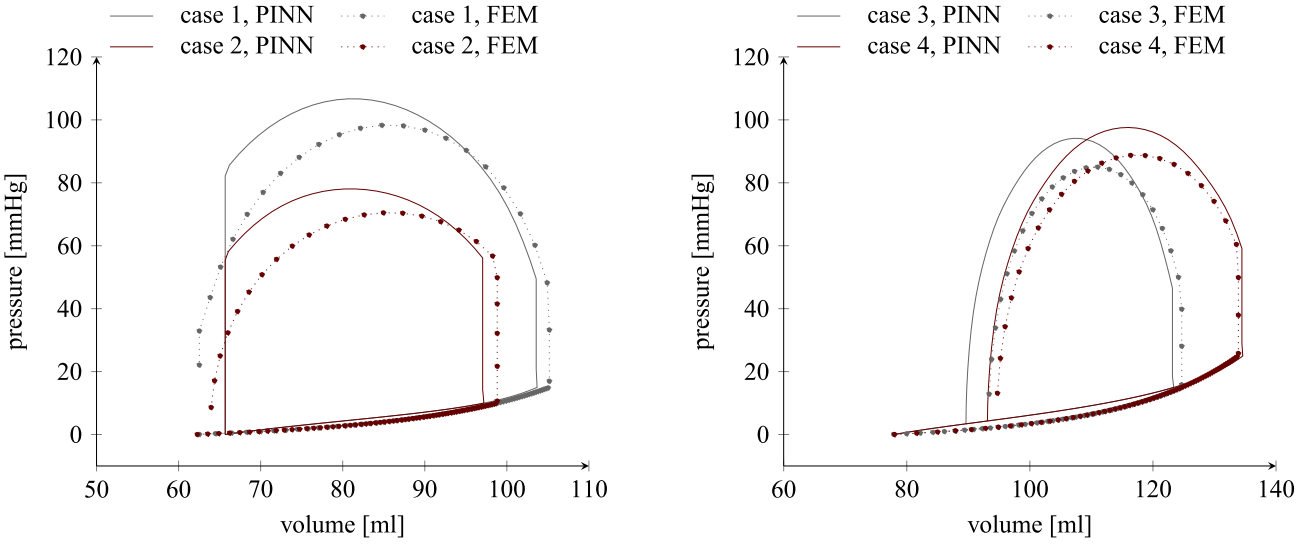

Fig. 7. Comparison of the pressure-volume curves for two anatomies out of the 10 comparison cases. Both operative conditions are plotted for each anatomy. Solid lines refer to the PINN predictions (network depth $m = 5$ and POD modes $N = 10$), dotted lines with symbols to the FEM solutions. Consistently with the average error predictions, we observe under-estimation of the EF, over-estimation of the PSV a larger SW in the PINN model. (For interpretation of the references to colour in this figure legend, the reader is referred to the web version of this article.)

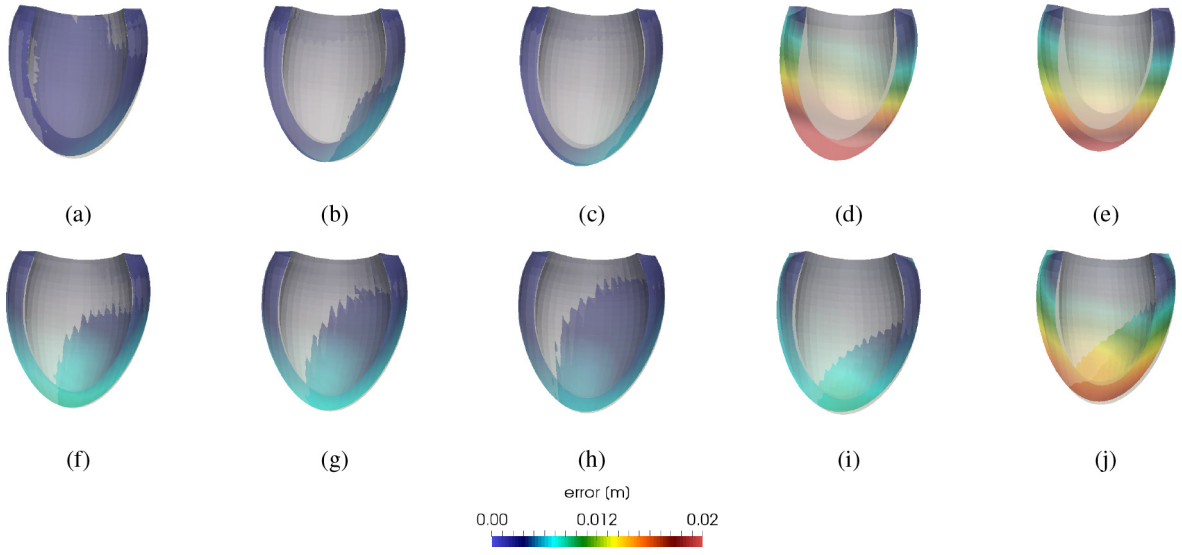

Fig. 8. Contours of prediction errors between PINN and FEM models for cases 2 (first row) and 4 (second row) of Fig. 7. Grey and colour shapes show the ground truth deformations predicted by FEM and the PINN error prediction, respectively for early diastole (a,f), mid diastole (b,g), end diastole (c,h), mid systole (d,i) and end systole (e,j). (For interpretation of the references to colour in this figure legend, the reader is referred to the web version of this article.)

the characteristic deformations of left-ventricular mechanics. This is obtained from a dataset of cardiac deformations from a biophysical Finite Element model on 100 synthetic geometries generated using the SM and realistic parameters for passive and active tissue properties, microstructure and systemic circulation. Using POD on the deformation fields, we generate a functional model (FM) encoding the dominant deformation features of left ventricles. Similarly to the SM, the first 5 modes retain 95% of the total energy of the deformations in the synthetic dataset. The projection matrix generated from the FM basis is used in the last, non-trainable layer of the network architecture to constrain the predicted deformation to be in the subspace of the FM.

Lastly, the PINN is trained using a cost function derived from the potential energy of the model constraining the network to provide a solution of the momentum conservation laws. The model only requires the definition of the anatomy and the assembly of the matrix for the calculation of the gradients of the displacements. It can then be trained without the need of input-output pairs thanks to the cost function selected.

We compared the predictions of the PINN with those from a FE biophysical model in 20 cases generated within the variability of the SM and FM. Model performance shows a large standard deviation of errors for 5 FM basis, which rapidly decrease when augmenting the size of the FM. We observed good accuracy in the metric of interest for the evaluation of left ventricle function, such as ejection fraction, maximum pressure and stroke work, with errors of -0.03 ± 0.05, 0.07 ± 0.06 and 0.04 ± 0.14, respectively, for 10 FM basis and 5 hidden layers. The largest contribution to the error predictions in the clinical metrics and strains are concentrated around the apex region (Fig. 8).

Further, end-diastolic strains show satisfactory agreement with the predictions from the biophysical model. For radial, longitudinal and circumferential strains, mean and standard deviation of the errors were -0.13 ± 0.12 -0.11 ± 0.10 and 0.14 ± 13, respectively.

These errors are within commonly reported ranges or ROMs where radial basis function are used. Recent work have also shown that such errors can potentially be corrected using statistical closure models for the PINN predictions as shown in the recent work of (Pagani et al., 2019). This will be the investigated in our future research efforts.

The network provides a significant reduction of the computational cost as compared to the FE model. For the calculation of one single operative condition the PINN is 30 times faster than the FE model when both run on the same CPU (Intel(R) Core(TM) i7-8700, 3.20 GHz). If we consider the computing times for multiple operative conditions for each anatomy, the PINN gain is even higher since the training is done only once and the solution time is around 1 min. These results come without any network optimization, and we believe these results could be further improved with a more refined network architecture.

In contrast to Maso Talou et al. (2020), our PINN needs to be trained for each new anatomy. We believe, however, that our approach offers several benefits. Firstly, the problem is regularised by including the physics at two levels, in the network architecture and in the cost function (Raissi, 2018). Additionally, despite requiring very short training times, our method allows for high flexibility in the variation of the PINN with respects to initial choices made before an expensive training process. In fact, parametric dependence on physiological and microstructural parameters can be easily included as inputs to the PINN, which can be re-trained in few minutes (assuming these inputs are within the variability of the parameters used for the generation of the FM). In this case, our preliminary experiments suggest that prediction performance could also be further increased by optimizing the network structure. Moreover, additional physical aspects can be included in the model by modifying the cost function (and the FM) appropriately. It is possible, for example, to include the effect of pericardium by prescribing an additional traction term in Eq. (6).

The PINN could be used in many applications where the speed of the calculation is more important than an accurate pointwise metric prediction. It will enormously speed up the calculation of activation stresses from clinical data as in the approach from Finsberg et al. (2018). Additionally, we believe the approach could be used for computationally cheap yet physiological realistic data augmentation, potentially allowing for training better classification, segmentation and generative models down stream. A third potential application is the use of the energy based cost function proposed as a physically informed regulariser, for example in predicting meshes from tagged MRI data.

5. Limitations

The model is based on a SM defined from an input dataset of limited dimension. A generalization to clinical applications of this work will require to extend the variability of anatomical shapes used as input to the SM. Additionally, although we observed that the SM bases derived can efficiently express anatomical variability in healthy and global diseased conditions (Joyce et al., 2020), the large impact of basis 2 (Fig. 4) suggests an inconsistency on the definition of the orientation of the cut plane. This approach allows to observe the same modes of variations presented in previous works but, nevertheless, alternative approaches for shape alignment and processing should be considered (Zhang et al., 2014; Lewandowski et al., 2013).

Additionally, an extended dataset would allow to quantify the probability of the distribution of the weights for the generation of synthetic anatomies. The MMWHS does not contain specific labels for the clinical status of the anatomies provided, therefore we could not differentiate SM weights distributions for the different conditions. Knowledge on the probability distributions of the SM weights for healthy and pathological cases would allow to train dedicated PINNs. The SM also hinges on bases modelling mostly global anatomical features. Therefore, it is well suited to represent healthy cases or global cardiac conditions, such ad dilated cardiomyopathy and hypertrophy. Including anatomies with local mechanical defects, such as scars, would require the use of a much larger set of modes.

We also consider here simplified electrophysiological and mechanical models, neglecting potential actuation dynamics in the anatomy and the presence of the pericardium. Although our approach has shown discriminating features between healthy and diseased heart conditions (Finsberg et al., 2018; Balaban et al., 2017), it would be very interesting for clinical applications to include local defects in the electrophysiological response of the ventricle and the constraining effect of pericardium. Our modelling assumptions are not constrained by limitations in our approach, but they are only done to limit the computational cost of this first investigation on the PINN performance for cardiac mechanic modelling. The effect of these assumptions will be inherently encoded in the FM bases, which are generated to provide a low-rank approximation of the deformation fields computed with such model. Selecting different boundary conditions and modelling strategies would only require to modify the cost function and generate a new set of FM bases. Finally, our investigation is limited to a small number of bases for the FM. While this shows good accuracy when compared to the FEM model, it certainly results in higher errors when considering local strains in the anatomy and apex displacements. To allow a sector-wise local evaluation of ventricular contraction and deformation, more bases should be included and, in this case, appropriate network sizing and architecture design are mandatory.

6. Conclusion

We propose a physics-informed neural network for personalized simulations of left ventricular mechanics. To the authors' knowledge, this is the first time personalised PINN are applied to cardiac mechanics. The network is constrained to produce deformation fields contained in the subspace of radial bases of a functional model encoding characteristic deformation of left ventricular anatomies. Additionally, the network is trained with a physics-based cost function that does not require input-output solutions pairs. The network, when compared to the corresponding biophysical Finite Element models, yields 30-fold reduction in compute time while ensuring good approximation of metrics of clinical interest.

Declaration of Competing Interest

The authors declare that they have no known competing financial interests or personal relationships that could have appeared to influence the work reported in this paper.

CRediT authorship contribution statement

Stefano Buoso: Conceptualization, Methodology, Software, Validation, Writing - original draft, Writing - review & editing. **Thomas Joyce:** Methodology, Software, Validation, Writing - review & editing. **Sebastian Kozerke:** Supervision, Writing - review & editing, Resources, Funding acquisition.

Acknowledgements

The authors acknowledge the financial support of the Swiss National Science Foundation (SNF) [Grant CR23I3-166485], and of PHRT SWISSHEART Failure Network of the ETH Domain.

References

Abadi, M., Agarwal, A., Barham, P., Brevdo, E., Chen, Z., Citro, C., Corrado, G. S., Davis, A., Dean, J., Devin, M., Ghemawat, S., Goodfellow, I., Harp, A., Irving, G., Isard, M., Jia, Y., Jozefowicz, R., Kaiser, L., Kudlur, M., Levenberg, J., Mané, D., Monga, R., Moore, S., Murray, D., Olah, C., Schuster, M., Shlens, J., Steiner, B., Sutskever, I., Talwar, K., Tucker, P., Vanhoucke, V., Vasudevan, V., Viégas, F., Vinyals, O., Warden, P., Wattenberg, M., Wicke, M., Yu, Y., Zheng, X., 2015. TensorFlow: Large-scale machine learning on heterogeneous systems. Software available from tensorflow.org. https://www.tensorflow.org/.

Abbasi-Sureshjani, S., Amirrajab, S., Lorenz, C., Weese, J., Pluim, J., Breeuwer, M., 2020. 4D semantic cardiac magnetic resonance image synthesis on xcat anatomical model. arXiv preprint arXiv:2002.07089

Alnæs, M.S., Blechta, J., Hake, J., Johansson, A., Kehlet, B., Logg, A., Richardson, C., Ring, J., Rognes, M.E., Wells, G.N., 2015. The FEniCS project version 1.5. Arch. Numer. Softw. 3 (100). doi:10.11588/ans.2015.100.20553.

Balaban, G., Finsberg, H., Odland, H.H., Rognes, M.E., Ross, S., Sundnes, J., Wall, S., 2017. High-resolution data assimilation of cardiac mechanics applied to a dyssynchronous ventricle. Int. J. Numer. Methods Biomed. Eng. 33 (11), e2863. doi:10.1002/cnm.2863.

Bernard, O., Lalande, A., Zotti, C., Cervenansky, F., Yang, X., Heng, P.-A., Cetin, I., Lekadir, K., Camara, O., Ballester, M.A.G., et al., 2018. Deep learning techniques for automatic MRI cardiac multi-structures segmentation and diagnosis: is the problem solved? IEEE Trans. Med. Imaging 37 (11), 2514–2525. doi:10.1109/TMI.2018.2837502.

Bonet, J., 2001. Large strain viscoelastic constitutive models. Int. J. Solids Struct. 38. doi:10.1016/S0020-7683(00)00215-8.

Bonet, J., Wood., R., 2008. Nonlinear Continuum Mechanics for Finite Element Analysis. Cambridge University Press, Cambridge, UK doi:10.1017/CBO9780511755446.

Buoso, S., Joyce, T., Kozerke, S., 2020. An MRI image-guided left-ventricular shape model embedding local physiological coordinates and directions. In: Proceedings of the International Society for Magnetic Resonance in Medicine 28, p. 2217.

Buoso, S., Manzoni, A., Alkadhi, H., Plass, A., Quarteroni, A., Kurtcuoglu, V., 2019. Reduced-order modeling of blood flow for noninvasive functional evaluation of coronary artery disease. Biomech. Model. Mechanobiol. 18 (6), 1867–1881. doi:10.1007/s10237-019-01182-w.

Buoso, S., Palacios, R., 2017. On-demand aerodynamics of integrally actuated membranes with feedback control. AIAA J. 55 (2), 377–388. doi:10.2514/1.J054888.

Carruth, E., McCulloch, A., Omens, J., 2016. Transmural gradients of myocardial structure and mechanics: implications for fiber stress and strain in pressure overload. Prog. Biophys. Mol. Biol. 122 (3), 215–226. doi:10.1016/j.pbiomolbio.2016.11.004.

Caruel, M., Chabiniok, R., Moireau, P., Lecarpentier, Y., Chapelle, D., 2014. Dimensional reductions of a cardiac model for effective validation and calibration. Biomech. Model. Mechanobiol. 13 (4), 897–914. doi:10.1007/s10237-013-0544-6.

Chabiniok, R., Wang, V.Y., Hadjicharalambous, M., Asner, L., Lee, J., Sermesant, M., Kuhl, E., Young, A.A., Moireau, P., Nash, M.P., Chapelle, D., Nordsletten, D.A., 2016. Multiphysics and multiscale modelling, data-model fusion and integration of organ physiology in the clinic: ventricular cardiac mechanics. Interface Focus 6 (2), 20150083. doi:10.1098/rsfs.2015.0083.

Charlton, P.H., Mariscal Harana, J., Vennin, S., Li, Y., Chowienczyk, P., Alastruey, J., 2019. Modeling arterial pulse waves in healthy aging: a database for in silico evaluation of hemodynamics and pulse wave indexes. Am. J. Physiology-Heart Circ. Physiol. 317 (5), H1062–H1085. doi:10.1152/ajpheart.00218.2019.

Chollet, F., et al., 2015. Keras. https://keras.io.

Corral-Acero, J., Margara, F., Marciniak, M., Rodero, C., Loncaric, F., Feng, Y., Gilbert, A., Fernandes, J.F., Bukhari, H.A., Wajdan, A., Martinez, M.V., Santos, M.S., Shamohammdi, M., Luo, H., Westphal, P., Leeson, P., DiAchille, P., Gurev, V., Mayr, M., Geris, L., Pathmanathan, P., Morrison, T., Cornelussen, R., Prinzen, F., Delhaas, T., Doltra, A., Sitges, M., Vigmond, E.J., Zacur, E., Grau, V., Rodriguez, B., Remme, E.W., Niederer, S., Mortier, P., McLeod, K., Potse, M., Pueyo, E., Bueno-Orovio, A., Lamata, P., 2020. The 'digital twin to enable the vision of precision cardiology. Eur. Heart J. doi:10.1093/eurheartj/ehaa159.

Del Santo, N., Deparis, S., Pegolotti, L., 2020. Data driven approximation of parametrized PDEs by reduced basis and neural networks. J. Comput. Phys. doi:10.1016/j.jcp.2020.109550.

Fares, E., Schröder, W., 2002. A differential equation for approximate wall distance. Int. J. Numer. Methods Fluids 39 (8), 743–762. doi:10.1002/fld.348.

Farrar, G., Suinesiaputra, A., Gilbert, K., Perry, J.C., Hegde, S., Marsden, A., Young, A.A., Omens, J.H., McCulloch, A.D., 2016. Atlas-based ventricular shape analysis for understanding congenital heart disease. Prog. Pediatr. Cardiol. 43, 61–69. doi:10.1016/j.ppedcard.2016.07.010. Proceedings of 2015 Innovations in Pediatric Heart Failure Symposium

Finsberg, H., 2017. Patient-Specific Computational Modeling of Cardiac Mechanics. University of Oslo Ph.D. thesis.

Finsberg, H., Balaban, G., Ross, S., Hland, T.F., Odland, H.H., Sundnes, J., Wall, S., 2018. Estimating cardiac contraction through high resolution data assimilation of a personalized mechanical model. J. Comput. Sci. 24, 85–90. doi:10.1016/j.jocs.2017.07.013.

Fresca, S., Dede, L., Manzoni, A., 2020. A comprehensive deep learning-based approach to reduced order modeling of nonlinear time-dependent parametrized pdes. arXiv preprint arXiv:2001.04001

Hesthaven, J., Ubbiali, S., 2018. Non-intrusive reduced order modeling of nonlinear problems using neural networks. J. Comput. Phys. 363, 55–78. doi:10.1016/j.jcp.2018.02.037.

Holzapfel, G.A., Ogden, R.W., 2009. Constitutive modelling of passive myocardium: a structurally based framework for material characterization. Philos. Trans. R. Soc. A 367 (1902), 3445–3475. doi:10.1098/rsta.2009.0091.

Joyce, T., Buoso, S., Yeurong, X., Kozerke, S., 2020. A machine learning approach to left ventricle mesh prediction from multi-slice MR images. In: Proceedings of the International Society for Magnetic Resonance in Medicine, 28, p. 2230.

Joyce, T., Kozerke, S., 2019. 3D medical image synthesis by factorised representation and deformable model learning. In: International Workshop on Simulation and Synthesis in Medical Imaging. Springer, pp. 110–119. doi:10.1007/978-3-030-32778-1_12.

Kingma, D. P., Ba, J., 2014. Adam: A method for stochastic optimization. arXiv preprint arXiv:1412.6980

Lee, K., Carlberg, K.T., 2020. Model reduction of dynamical systems on nonlinear manifolds using deep convolutional autoencoders. J. Comput. Phys. 404, 108973. doi:10.1016/j.jcp.2019.108973.

Lewandowski, A.J., Augustine, D., Lamata, P., Davis, E.F., Lazdam, M., Francis, J., McCormick, K., Wilkinson, A.R., Singhal, A., Lucas, A., Smith, N.P., Neubauer, S., Leeson, P., 2013. Preterm heart in adult life. Circulation 127 (2), 197–206. doi:10.1161/CIRCULATIONAHA.112.126920.

Logg, A., Mardal, K.-A., Wells, G.N., et al., 2012. Automated Solution of Differential Equations by the Finite Element Method. Springer doi:10.1007/978-3-642-23099-8.

Mancinella, C., Livesub, M., Puppoa, E., 2019. A comparison of methods for gradient field estimation on simplicial meshes. Comput. Graph. 80, 37–50. doi:10.1016/j.cag.2019.03.005.

Manzoni, A., Quarteroni, A., Rozza, G., 2012. Model reduction techniques for fast blood flow simulation in parametrized geometries. Int. J. Numer. Methods Biomed. Eng. 28 (6-7), 604–625. doi:10.1002/cnm.1465.

Maso Talou, G.D., Babarenda Gamage, T.P., Sagar, M., Nash, M.P., 2020. Deep learning over reduced intrinsic domains for efficient mechanics of the left ventricle. Front. Phys. 8, 30. doi:10.3389/fphy.2020.00030.

Mollro, R., Pennec, X., Delingette, H., Ayache, N., Sermesant, M., 2019. Population-based priors in cardiac model personalisation for consistent parameter estimation in heterogeneous databases. Int. J. Numer. Methods Biomed. Eng. 35 (2), e3158. doi:10.1002/cnm.3158.

Neic, A., Campos, F.O., Prassl, A.J., Niederer, S.A., Bishop, M.J., Vigmond, E.J., Plank, G., 2017. Efficient computation of electrograms and ECGs in human whole heart

simulations using a reaction-eikonal model. J. Comput. Phys. 346, 191–211. doi:10.1016/j.jcp.2017.06.020.
Nguyen-Thanh, V.M., Zhuang, X., Rabczuk, T., 2020. A deep energy method for finite deformation hyperelasticity. Eur. J. Mech. A/Solids 80, 103874. doi:10.1016/j.euromechsol.2019.103874.
Pagani, S., Manzoni, A., Carlberg, K., 2019. Statistical closure modeling for reduced-order models of stationary systems by the romes method. arXiv:1901.02792
Paun, B., Bijnens, B., Iles, T., Iaizzo, P.A., Butakoff, C., 2017. Patient independent representation of the detailed cardiac ventricular anatomy. Med. Image Anal. 35, 270–287. doi:10.1016/j.media.2016.07.006.
Pfaller, M.R., Cruz Varona, M., Lang, J., Bertoglio, C., Wall, W.A., 2020. Using parametric model order reduction for inverse analysis of large nonlinear cardiac simulations. Int. J. Numer. Methods Biomed. Eng. 36 (4), e3320. doi:10.1002/cnm.3320.
Pfaller, M.R., Hrmann, J.M., Weigl, M., Nagler, A., Chabiniok, R., Bertoglio, C., Wall, W.A., 2019. The importance of the pericardium for cardiac biomechanics: from physiology to computational modeling. Biomech. Model. Mechanobiol. 18, 503–529. doi:10.1007/s10237-018-1098-4.
Potse, M., Dube, B., Richer, J., Vinet, A., Gulrajani, R.M., 2006. A comparison of monodomain and bidomain reaction-diffusion models for action potential propagation in the human heart. IEEE Trans. Biomed. Eng. 43, 242–243. doi:10.1109/TBME.2006.880875.
Quarteroni, A., Rozza, G., 2007. Numerical solution of parametrized Navier–Stokes equations by reduced basis methods. Numer. Methods Partial Differ. Equ. 23 (4), 923–948. doi:10.1002/num.20249.
Raissi, M., 2018. Deep hidden physics models: deep learning of nonlinear partial differential equations. J. Mach. Learn. Res. 19, 1–24.
Ramachandran, P., Zoph, B., Le, Q. V., 2017. Searching for activation functions. arXiv preprint arXiv:1710.05941
Ronneberger, O., Fischer, P., Brox, T., 2015. U-net: Convolutional networks for biomedical image segmentation. In: International Conference on Medical image computing and computer-assisted intervention. Springer, pp. 234–241. doi:10.1007/978-3-319-24574-4_28.
Roth, B.J., Wikswo, J.P., 1986. A bidomain model for the extracellular potential and magnetic field of cardiac tissue. IEEE Trans. Biomed. Eng. 33, 467–469. doi:10.1109/TBME.1986.325804.
Rowley, C.W., 2011. Model reduction for fluids, using balanced proper orthogonal decomposition. Int. J. Bifurc. Chaos 15 (03), 997–1013. doi:10.1142/S0218127405012429.
Sack, K.L., Aliotta, E., Ennis, D.B., Choy, J.S., Kassab, G.S., Guccione, J.M., Franz, T., 2018. Construction and validation of subject-specific biventricular finite-element models of healthy and failing swine hearts from high-resolution DT-MRI. Front. Physiol. 9, 539. doi:10.3389/fphys.2018.00539.
Simo, J., Hughes, T., 1998. Computational Inelasticity. Springer: Interdisciplinary applied mathematics: Mechanics and materials, Springer-Verlag New York doi:10.1007/b98904.
Suinesiaputra, A., Ablin, P., Alb, X., Alessandrini, M., Allen, J., Bai, W., Imen, S., Claes, P., Cowan, B.R., D'hooge, J., Duchateau, N., Ehrhardt, J., Frangi, A.F., Gooya, A., Grau, V., Lekadir, K., Lu, A., Mukhopadhyay, A., Oksuz, I., Parajuli, N., Pennec, X., Pereaez, M., Pinto, C., Piras, P., Roh, M., Rueckert, D., Sring, D., Sermesant, M., Siddiqi, K., Tabassian, M., Teresi, L., Tsaftaris, S.A., Wilms, M., Young, A.A., Zhang, X., Medrano-Gracia, P., 2018. Statistical shape modeling of the left ventricle: myocardial infarct classification challenge. IEEE J. Biomed. Health Inform. 22 (2), 503–515. doi:10.1109/JBHI.2017.2652449.
Toussaint, N., Stoeck, C.T., Schaeffter, T., Kozerke, S., Sermesant, M., Batchelor, P.G., 2013. In vivo human cardiac fibre architecture estimation using shape-based diffusion tensor processing. Med. Image Anal. 17 (8), 1243–1255. doi:10.1016/j.media.2013.02.008.
Westerhof, N., Lankhaar, J., Westerhof, B., 2009. The arterial Windkessel. Med. Biol. Eng. Comput. 47 (2), 131–141.
Young, A.A., Frangi, A.F., 2009. Computational cardiac atlases: from patient to population and back. Exp. Physiol. 94 (5), 578–596. doi:10.1113/expphysiol.2008.044081.
Zhang, X., Cowan, B.R., Bluemke, D.A., Finn, J.P., Fonseca, C.G., Kadish, A.H., Lee, D.C., Lima, J.A.C., Suinesiaputra, A., Young, A.A., Medrano-Gracia, P., 2014. Atlas-based quantification of cardiac remodeling due to myocardial infarction. PLoS One 9 (10), 1–13. doi:10.1371/journal.pone.0110243.
Zhuang, X., 2013. Challenges and methodologies of fully automatic whole heart segmentation: a review. J. Healthc. Eng. 4 (3), 371–407. doi:10.1260/2040-2295.4.3.371.
Zhuang, X., Rhode, K.S., Razavi, R.S., Hawkes, D.J., Ourselin, S., 2010. A registration-based propagation framework for automatic whole heart segmentation of cardiac MRI. IEEE Trans. Med. Imaging 29 (9), 1612–1625. doi:10.1109/TMI.2010.2047112.
Zhuang, X., Shen, J., 2016. Multi-scale patch and multi-modality atlases for whole heart segmentation of MRI. Med. Image Anal. 31, 77–87. doi:10.1016/j.media.2016.02.006.